Available online at www.sciencedirect.com
ScienceDirect
Trans. Nonferrous Met. Soc. China 34(2024) 2756−2771
Transactions of Nonferrous Metals Society of China
www.tnmsc.cn

Microstructure, interfacial reaction behavior, and mechanical properties of Ti_3AlC_2 reinforced Al6061 composites

Zhi-bin LIU[1,2], Jia-bao BAO[1], Wen-jie HU[1], Hong YAN[1]

1. School of Advanced Manufacturing, Nanchang University, Nanchang 330031, China;
2. Jiangxi Vocational and Technical College of Communications, Nanchang 330013, China

Received 24 March 2023; accepted 28 September 2023

Abstract: The interfacial reaction behavior of Al and Ti_3AlC_2 at different pouring temperatures and its effect on the microstructure and mechanical properties of the composites were investigated. The results show that the addition of 3.0 wt.% Ti_3AlC_2 refines the average grain size of α(Al) in the composite by 50.1% compared to Al6061 alloy. Morphological analyses indicate that an in-situ Al_3Ti transition layer of ~180 nm in thickness is generated around the edge of Ti_3AlC_2 at 720 °C, forming a well-bonded Al−Al_3Ti interface. At this processing temperature, the ultimate tensile strength of Al6061−3.0 wt.%Ti_3AlC_2 composite is 199.2 MPa, an improvement of 41.5% over the Al6061 matrix. Mechanism analyses further elucidate that 720 °C is favourable for forming the nano-sized transition layer at the Ti_3AlC_2 edges. And, the thermal mismatch strengthening plays a dominant role in this state, with a strengthening contribution of about 74.8%.

Key words: Al6061 composites; Ti_3AlC_2; microstructure; interfacial reaction; tensile mechanical properties

1 Introduction

Al6061 alloy is one of the heat treatable wrought aluminum alloys, which is widely used for various brackets, heat exchangers and structural components owing to its excellent plasticity, weldability and corrosion resistance [1]. However, Al6061 alloy does not have sufficient strength and significant wear resistance, thus limiting its engineering applications especially in high load or high temperature environments. To date, some traditional ceramics, such as Al_2O_3 [2], SiC [3], and B_4C [4] are widely used as reinforcements for aluminum matrix composites (AMCs) due to their high strength and hardness. Unfortunately, these non-deformable ceramic reinforcements are brittle, predisposing to low plasticity and early failure of the composites. As a class of kinking nonlinear elastic reinforcements, MAX phases have attracted widespread attention since their first launch. The unique nano-layered crystal structure endows the MAX phases with excellent ceramic-like and metal-like properties, such as high elastic modulus, easy machinability and good thermal conductivity [5]. Hence, the MAX phases are considered to be ideal reinforcements for optimising the microstructure and mechanical properties of different metal matrices.

Titanium aluminum carbide (Ti_3AlC_2) is one of the typical representatives of the MAX phases, with the optimum oxidation resistance and processability among the MAX phases reported so far [6]. However, studies on this phase reinforced AMCs are very limited, probably due to the poor wettability of Ti_3AlC_2 with the molten metal. In recent years, attempts devoted to the preparation of Al−Ti_3AlC_2 composites by casting process are also

Corresponding author: Hong YAN, Tel: +86-791-83969622, E-mail: hyan@ncu.edu.cn
DOI: 10.1016/S1003-6326(24)66574-X

emerging. ZHAI et al [7] investigated the influence of Ti_3AlC_2 contents on the tribological behaviors of the composites produced by agitation casting at 750 °C. The results indicated that the porosity of the composites increases with increasing reinforcement content, which may be caused by the weak bonding interface between Ti_3AlC_2 and the Al matrix. In addition, it is easy to find that the content of Ti_3AlC_2 in Al−Ti_3AlC_2 composites prepared by powder metallurgy process is 10.0−35.0 wt.% [8,9], which is much more than the casting process (<5.0 wt.%). However, the porosity of the composites increases with increasing reinforcement content due to the mechanical infiltration between the reinforcement and the Al matrix, rather than ionic adsorption or interfacial reactions. Therefore, electroless coating has been used to enhance the interfacial bonding strength between the Ti_3AlC_2 and the matrix. But, it will inevitably lead to a complicated preparation process.

Amazingly, the structure of Ti_3AlC_2 is typified by strong covalent Ti—C bonds intercalated with Al layers via weaker Ti—Al bonds, which spawned an innovative idea for the preparation of in-situ AMCs. WANG et al [9] prepared Ti_3AlC_2−Al_3Ti aluminium composites using hot-press sintering at 780 °C. Their findings revealed that the Ti atoms around the edges of Ti_3AlC_2 would diffuse into Al matrix and then react with Al atoms to form in-situ Al_3Ti, which is tightly combined with Al, thus strengthening the interface. WANG et al [10] researched the ductility of Ti_3AlC_2/Al composites prepared with spark plasma sintering. Their finding indicated that the Al_3Ti whiskers, which can improve the interfacial bonding strength, are formed on the surface of Ti_3AlC_2 phases when the sintering temperature ≥620 °C. Moreover, it has been shown that Al_3Ti has a good lattice match with Al and may act as a non-homogeneous nucleation site during solidification of molten Al, thus improving the interfacial bonding with the Al matrix [11]. These studies are good inspirations for inducing the in-situ Al_3Ti generated on the surface of the Ti_3AlC_2 phases by properly controlling the reaction temperature, which in turn promotes the synergistic reinforcement of Ti_3AlC_2−Al_3Ti to AMCs. However, the reaction temperature for generating optimum Al_3Ti grain size and content requires precise control. Also, this concept has rarely been investigated in the casting process, even though the process is a relatively low cost and easy industrial production method for manufacturing complex structural parts. Therefore, it is meaningful and challenging to investigate the interfacial strengthening of Ti_3AlC_2 in molten AMCs.

In this study, the Al6061−Ti_3AlC_2 composites were fabricated by ultrasonic-assisted casting. The effects of different Ti_3AlC_2 contents on the micromorphology of Al6061 composites were studied. Based on this, the interfacial reaction of Al and Ti_3AlC_2 at different pouring temperatures and its effect on the mechanical properties of the Al6061 composites were investigated. Finally, the reaction and strengthening mechanisms of Ti_3AlC_2 on Al6061 composites were discussed as well.

2 Experimental

2.1 Materials

Commercially available Al6061 alloy was selected as the matrix. Table 1 shows the chemical composition of the matrix measured by an optical emission spectrometer (OES). Ti_3AlC_2 particles were used as the reinforcement, and the synthesis process was referred to the previous study [12]. Firstly, the Ti, Al, C and Sn powders with a molar ratio of 3∶1∶1.8∶0.2 were well-dispersed by magnetic stirring for 1 h in ethanol solution and then drying at 75 °C under 1 kPa. After that, the proportioned powders were mixed by ball milling for 3 h at 300 r/min. The well-mixed powders were cold-pressed into a *d*40 mm compact under 105 MPa, and then put into a vacuum tube furnace with a ceramic boat for calcining at 1400 °C under a 5 mPa vacuum, with a holding time of 20 min. The prepared Ti_3AlC_2 compact was finally ground and sifted through a 500 mesh sieve to get the fine particles. Figure 1 illustrates the specific fabrication process of this experiment.

Table 1 Chemical composition of Al6061 alloy (wt.%)

Mg	Si	Fe	Cu	Cr	Mn	Zn	Ti	Al
0.99	0.55	0.33	0.20	0.12	0.10	0.08	0.03	Bal.

2.2 Fabrication of Al6061−Ti_3AlC_2 composites

Referring to the findings of ZHAI et al [7] and YU et al [13], the addition of Ti_3AlC_2 was set as 2.0, 3.0 and 4.0 wt.% in this experiment, respectively. Hereafter, AT2.0, AT3.0 and AT4.0 were used as

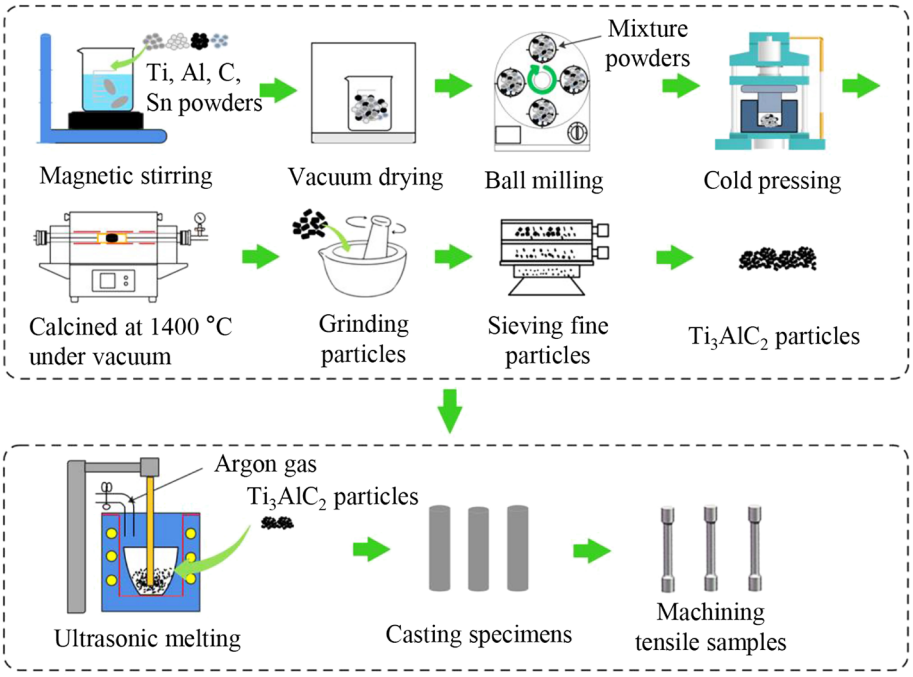

Fig. 1 Schematic diagram of fabrication process of Al6061−Ti_3AlC_2 composites

the designations of the composites. The Al6061 alloy was heated to 750 °C in a resistance furnace until complete melting, and then held for 20 min. Thereafter, the melt temperature was cooled to 700, 720 and 740 °C, respectively, and then a specific amount of Ti_3AlC_2 particles were successively added into the Al6061 melt. To disperse the Ti_3AlC_2 particles uniformly in the melt, high-intensity sonication was performed at 2.8 kW ultrasonic power for 10 min. Also, an argon atmosphere was employed to prevent the oxidation of Ti_3AlC_2 particles and molten Al during the process. Subsequently, the melt was poured into a preheated steel die (~200 °C) with dimensions of *d*10 mm × 150 mm, and then air-cooled to produce the designed composites.

2.3 Characterization

The phase transitions of the raw materials and the prepared composites were identified by an X-ray diffraction (XRD, Rigaku, Japan). The specimens of different Al6061−Ti_3AlC_2 composites were polished by Al_2O_3 suspension with a particle size of 0.5 μm, and then etched with a 0.5 vol.% hydrofluoric acid solution. The microstructure, phase composition and fracture morphology were examined by a scanning electron microscope equipped with an energy-dispersive spectrometer (SEM, Tescan-Vega3, China). The micro-interface structure between Al and Ti_3AlC_2 was observed by a transmission electron microscope (TEM, JEM−2100F, Japan).

2.4 Evaluation of mechanical properties

Mechanical properties of the Al6061 and the prepared composites were evaluated for Vickers hardness and tensile strength. The Vickers hardness was measured with a micro-hardness tester (HVX−1000A, China) at a load of 1.96 N with a holding time of 15 s. Seven random measurements were taken on each sample to ensure confidence in the data. In addition, the hardness (H_V) of the composites was calibrated by the ratio of the load F (N) to the area S (mm^2) in contact between the indenter and the material. The equation is shown as Eq. (1) [14], where D (mm) is the average size of the measured diagonal of the indentation.

$$H_V=F/S\approx0.1891F/D^2 \quad (1)$$

The room temperature tensile tests were performed on a universal testing machine (UTM5105, China) at a strain rate of 0.5 mm/min. The casting specimens were machined into tensile test bars of *d*6 mm and 60 mm in gauge length. Five test bars were randomly selected for each sample, and average test was taken to support the performance calibration.

3 Results and discussion

3.1 Phase analyses and microstructures

3.1.1 Phase analyses of Ti_3AlC_2 and composites

Figure 2 shows the secondary electron SEM image and the XRD pattern of the Ti_3AlC_2 particles. These particles are irregularly shaped with an average size of 6.24 μm and an aspect ratio of 1.86, as well as the typical three-dimensional layered morphology of Ti_3AlC_2 can be clearly observed in the upper right corner of Fig. 2(a). XRD analysis shows that the diffraction peaks index mainly to the Ti_3AlC_2 phases (JCPDS No. 52-0875), and only faint TiC crystalline impurity peaks are detected, as shown in Fig. 2(b). This suggests that the composition of Ti_3AlC_2 prepared under this experimental conditions can be guaranteed.

Figure 3(a) depicts the XRD patterns of Al6061−Ti_3AlC_2 composites poured at 740 °C. It can be noted that these composites consist mainly of four phases: Al, Al_8Fe_2Si, Mg_2Si, and Ti_3AlC_2, which is consistent with previous studies [15]. In addition, the XRD patterns show weaker Al_3Ti diffraction peaks when the addition content is greater than 3.0 wt.%. This indicates that Ti_3AlC_2 is effectively compounded into the matrix under experimental conditions and reacts with Al to form in-situ Al_3Ti. Figure 3(b) shows the XRD patterns of AT3.0 composites poured at 700, 720 and 740 °C. Only diffraction peaks of the added Ti_3AlC_2 phases are detected at pouring temperatures of 700 and 720 °C, except for the Al6061 alloy composition. As the temperature increases to 740 °C, weak Al_3Ti peaks can be observed in the XRD pattern. It is worth stating that this differs from the findings of WANG et al [9], where no Al_4C_3 is detected in the present study. We speculate that this is related to the poor or even absence of reaction between Ti_3AlC_2 and Al at lower temperatures, and to the fact that the content of Al_4C_3 generated by this reaction is much lower, so that it cannot be detected in XRD.

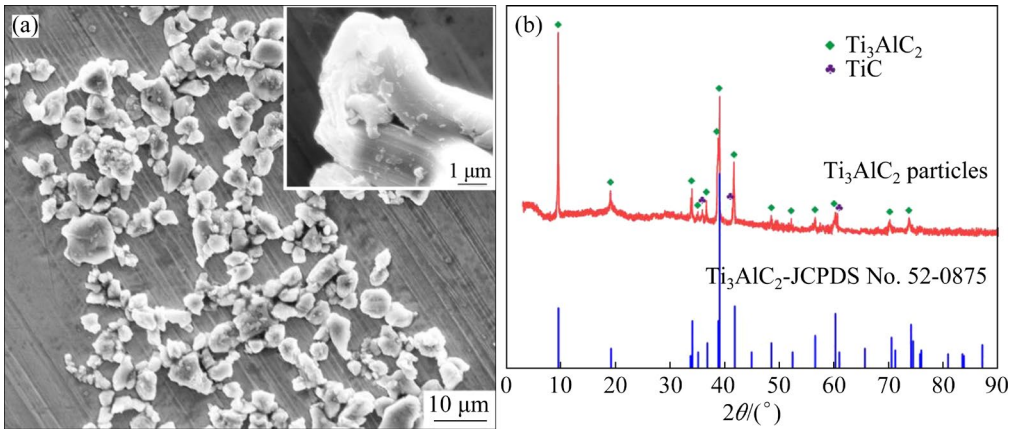

Fig. 2 SEM image (a) and XRD pattern (b) of Ti_3AlC_2 particles

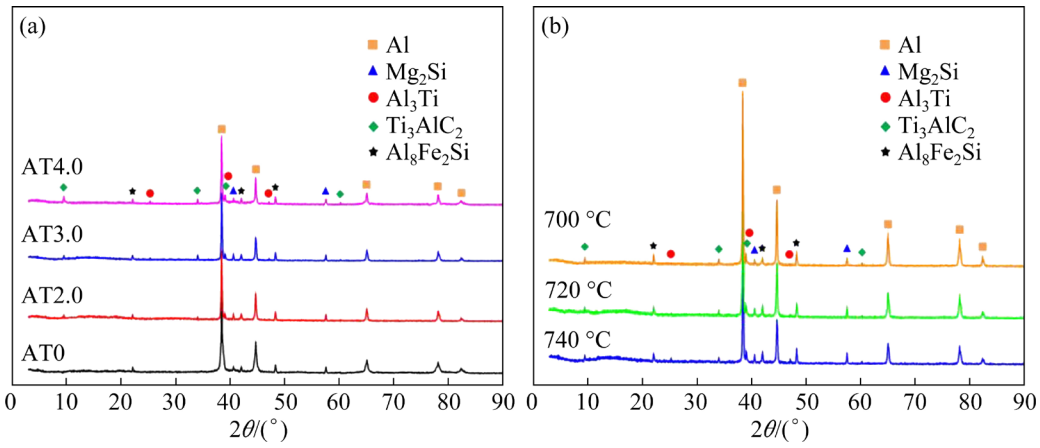

Fig. 3 XRD patterns of Al6061−Ti_3AlC_2 composites poured at 740 °C (a) and AT3.0 composite poured at different temperatures (b)

With the above XRD results, we can tentatively assume that as the temperature increases, more Ti_3AlC_2 reacts with Al and eventually produces more in-situ Al_3Ti. Therefore, it is conceivable to control the interfacial reaction behavior between Al and Ti_3AlC_2 via adjusting the pouring temperature.

3.1.2 Microstructures of Al6061−Ti_3AlC_2 composites

Figure 4 illustrates the back-scatter SEM images of Al6061 and the Al6061−Ti_3AlC_2 composites at pouring temperature of 740 °C. As shown in Fig. 4(a), the as-cast Al6061 mainly consists of coarse primary α(Al) grains, and the

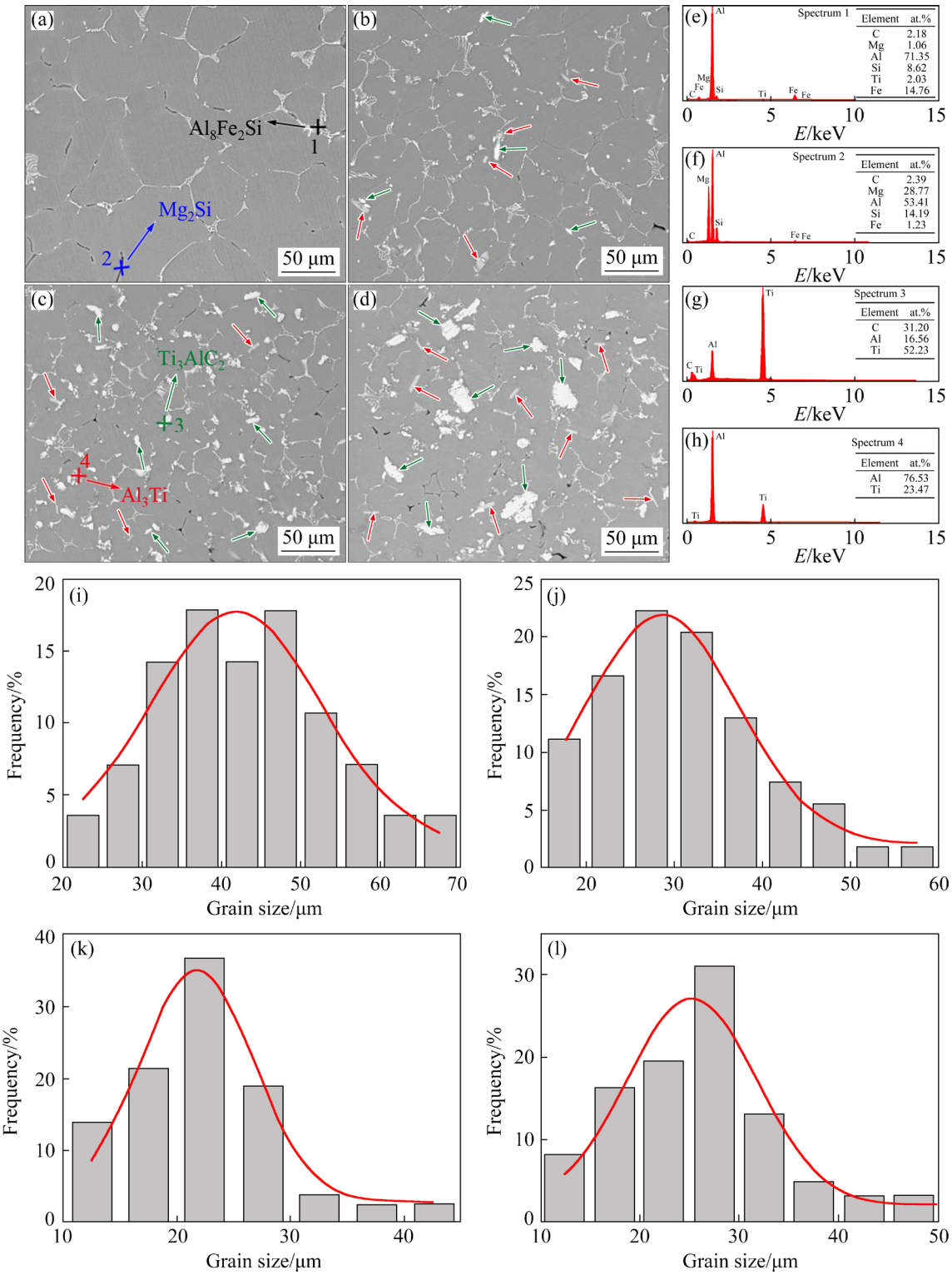

Fig. 4 SEM images of samples at pouring temperature of 740 °C: (a) AT0; (b) AT2.0; (c) AT3.0; (d) AT4.0; (e−h) EDS results of Spectra 1, 2, 3 and 4, respectively; (i−l) Grain size distribution of (a−d), respectively

second phases are distributed in a non-continuous network along the grain boundaries. The EDS results of Spectra 1 and 2 are shown in Figs. 4(e) and (f) and are presumed to be Al_8Fe_2Si and Mg_2Si according to their atomic ratios [15,16]. Figures 4(b−d) clearly show that the glossy white particles are uniformly distributed in the matrix, with a few light grey rods scattered nearby, as marked by the green and red arrows, respectively. EDS analyses (Figs. 4(g) and (h)) confirm that the atomic ratios of the two mentioned substances are similar to those of Ti_3AlC_2 and Al_3Ti phases [9,10], respectively. This indicates that when the pouring temperature increases to 740 °C, the Ti element in Ti_3AlC_2 readily reacts with the Al element in the matrix to form in-situ Al_3Ti. Moreover, the average grain size of Al6061 matrix is 43.8 μm as measured by Image J analysis software. As the Ti_3AlC_2 content increases from 2.0 wt.% to 3.0 wt.%, and then to 4.0 wt.%, the size of primary α(Al) refines significantly, with reduction of 31.2%, 50.1% and 40.9%, respectively (Figs. 4(i−l)). This may be due to the uniformly dispersed Ti_3AlC_2 particles and the lattice coherency between Al and in-situ Al_3Ti, which acts as a good heterogeneous nucleation, and thus effectively inhibits the growth of α(Al) grains. In addition, a partial agglomeration of Ti_3AlC_2 is present in Fig. 4(d), and more rod-like Al_3Ti phases are observed compared with Figs. 4(b) and (c). Therefore, considering the refining effect of α(Al) grains and the dispersion of Ti_3AlC_2, we presume an optimal addition of 3.0 wt.%.

To further compare the reaction degree between Ti_3AlC_2 and Al at different pouring temperatures, SEM morphologies of AT3.0 composites at 700, 720 and 740 °C are observed, as shown in Fig. 5. The Ti_3AlC_2 particles tend to distribute around the α(Al) grain boundaries. In Fig. 5(a), no visible light gray phase is observed along the edges of the Ti_3AlC_2 particles, suggesting that the interfacial reaction may not occur at 700 °C. In Fig. 5(b), a faint nascent light gray phase can be observed along the edges of a few Ti_3AlC_2 particles, which could be the Al_3Ti detected in Fig. 4. In contrast, the average length of in-situ Al_3Ti reaches 7.6 μm and its content increases significantly when the pouring temperature is increased to 740 °C (Fig. 5(c)). The average volumes of Ti_3AlC_2 and Al_3Ti are calculated by distinguishing the contrasting difference of the various phases in Figs. 5(a−c) using a software of Image-Pro Plus. The results show that the volumes of Ti_3AlC_2 are 2.4%, 2.2% and 1.7%, and the volumes of Al_3Ti are 0, 0.4% and 1.0% at temperatures of 700, 720 and 740 °C, respectively.

Figure 5(d) shows the EDS mapping results corresponding to Fig. 5(c). From the elemental distribution of Al, Ti and C in the region where the reinforcement phases are located, the distribution areas of Ti and Al elements are larger than that of C element, which may be due to the formation of an in-situ Al_3Ti layer at the outer edge of Ti_3AlC_2 particles during the reaction. This phenomenon of in-situ Al_3Ti generated at the boundary of Ti_3AlC_2 particles is consistent with the previous findings [10]. It is noteworthy that the rod-like gray phases can be observed from Fig. 5(c) and its mapping results, which is consistent with the

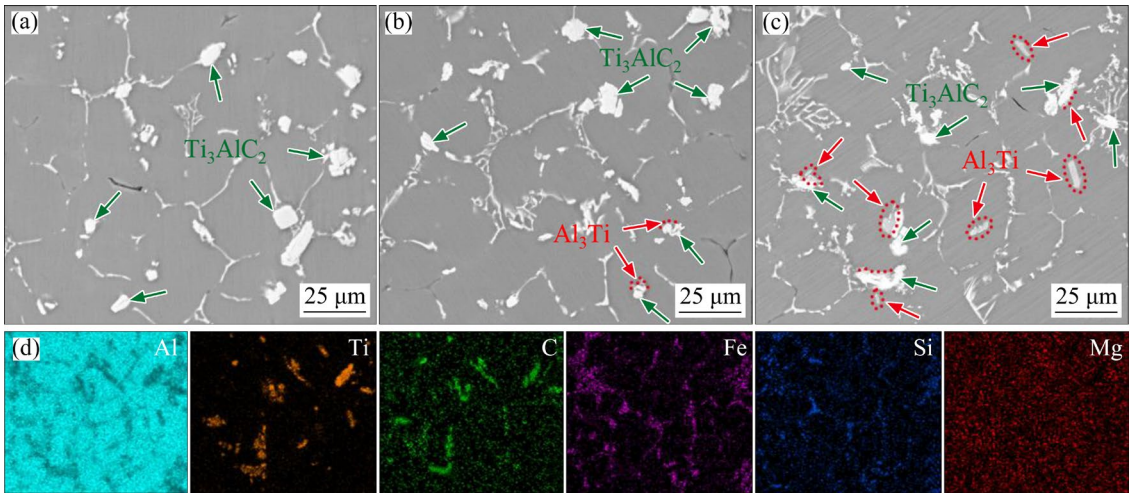

Fig. 5 SEM images of AT3.0 composites at various pouring temperatures: (a) 700 °C; (b) 720 °C; (c) 740 °C; (d) EDS mappings of (c)

observation in Fig. 4. This may be due to the fact that Al atoms preferentially react with Ti atoms along the edge of Ti_3AlC_2, which has a smaller distribution than Al atoms. Therefore, Al_3Ti generated by the reaction is more inclined to grow in strips along the edge of Ti_3AlC_2 particles.

Figure 6 shows SEM images and line scan results of the composites fabricated at 740 °C. It can be observed that the intensity fluctuations of the Al, Ti and C elements are across the interface. In the glossy white areas, the intensity of Ti is stronger than that of Al, and the peak intensity of C is also stronger. In the light grey area, the intensity of the peaks for the elements Al and Ti are opposite, and the C peak is weaker. As a result, it can be further speculated that the reaction at the interface between the reinforcements and the 6061 matrix produces the in-situ Al_3Ti measured in Fig. 4.

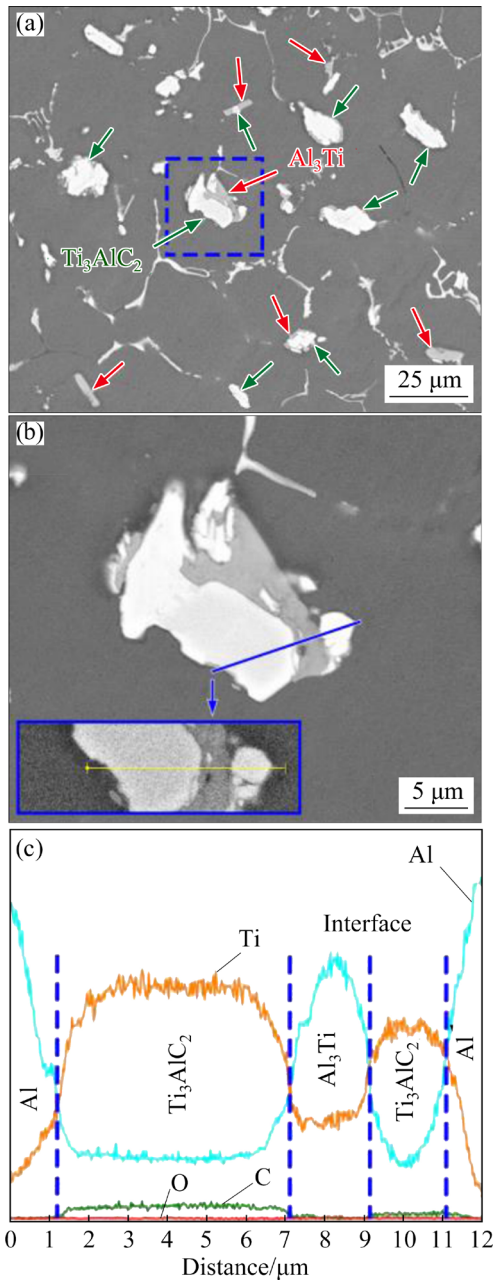

Fig. 6 SEM images of AT3.0-740 °C composite (a, b), and elemental line scan results (c) marked in (b)

Figure 7 shows TEM images of AT3.0-720 °C composite. As shown in Fig. 7(a), a colour difference nascent phase is distributed at the Al−Ti_3AlC_2 interface, with a layer thickness of ~180 nm. Figure 7(c) shows the EDS results of the selected areas 1 and 2 in Fig. 7(a), it can be tentatively identified that the reaction layer is composed of in-situ Al_3Ti. In addition, the EDS mappings of Al, Ti and C of Fig. 7(a) are shown in Fig. 7(d), indicating that there is no enrichment of elemental C in the nascent phase at the Ti_3AlC_2 edges. Figure 7(b) illustrates the HRTEM morphology and selective area electron diffraction (SAED) patterns of the Zones *A* and *C*. The lattice spacings of Zone *A* are 0.2732 and 0.4297 nm, respectively, which could originate from the (110) and (002) facets of Al_3Ti with a crystal axis of $[\bar{1}10]$. Similarly, the lattice spacings of the two crystal facets in the Zone *C* are 0.2340 and 0.2341 nm, identical to the $(1\bar{1}\bar{1})$ and (111) crystal facets of Al and align along the $[01\bar{1}]_{Al}$ crystal axis. Therefore, combining the EDS analyses and SAED patterns, it can be further identified that nano-sized Al_3Ti is generated around the edges of Ti_3AlC_2, and the corresponding reactive transition layer is the Al−Al_3Ti interface.

In addition, a mutually embedded and clean Al−Al_3Ti interface is clearly observed in Fig. 7(b), indicating the presence of a strong interfacial bonding. Moreover, the blue box on the left of Fig. 7(b) shows the inverse fast Fourier transform (IFFT) image corresponding to the interface zone *B*, revealing the presence of a large number of dislocation tangles near the interface layer (marked as "T"). This may be due to the good lattice match between nano-sized Al_3Ti and Al [11]. On the one hand, it promotes bridging between Al and Ti_3AlC_2, and induces load transfer from Al_3Ti to Ti_3AlC_2 through the Al−Al_3Ti interface. On the other hand, it also effectively accumulates interfacial dislocations and relieves stress concentration.

Based on the above analyses, it can be noticed that when the pouring temperature is lower than 700 °C, no visible interfacial reaction occurs

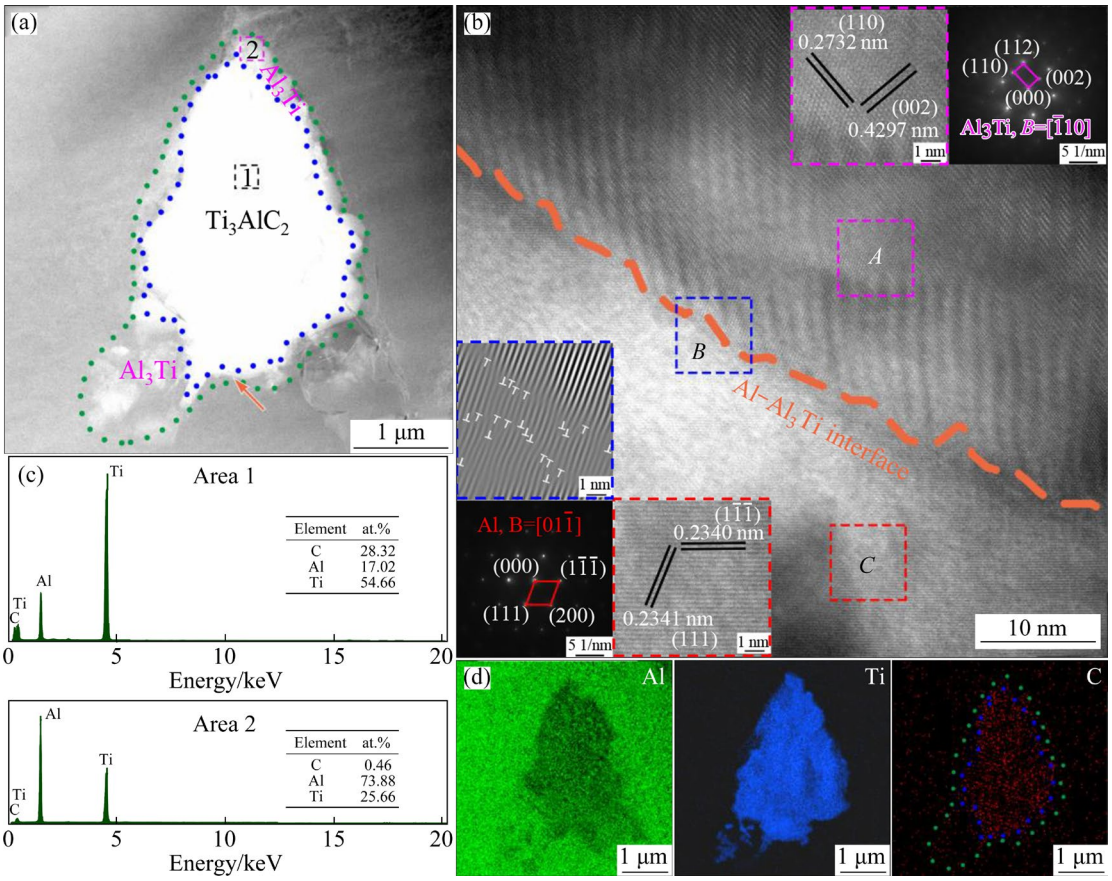

Fig. 7 (a) TEM image; (b) HRTEM morphology; (c) EDS results of Areas 1 and 2 in (a); (d) EDS mappings of Al, Ti and C for (a)

between Al and Ti_3AlC_2. As the temperature increases to 720 °C, the interfacial reaction induces and generates in-situ Al_3Ti. Thereafter, the grain size and content of Al_3Ti increase as the temperature continues to increase. Besides, it is demonstrated that the following interfacial reaction between Al and Ti_3AlC_2 exists during hot-press sintering at 780 °C [9].

$$3Ti_3AlC_2+32Al\rightarrow 2Al_4C_3+9Al_3Ti \quad (2)$$

With the beginning of the reaction, Al atoms in the matrix react with Ti atoms in the reinforcement to form the in-situ Al_3Ti, consuming part of the Ti atoms in Ti_3AlC_2, but its original crystal structure remains unchanged. As the temperature increases, the reaction between Al and Ti_3AlC_2 intensifies due to the increase in thermal energy, and part of the Ti_3AlC_2 reacts completely with Al. However, comparing with results obtained by WANG et al [9] at 780 °C sintering, the present study is able to produce Al_3Ti with an average grain size below 180 nm at 720 °C, which is mainly linked to the two potential factors. On the one hand, the liquid α(Al) surrounds Ti_3AlC_2 particles at high temperature, providing a path for the diffusion of Al atoms [17]. On the other hand, the transient and local high temperature and pressure triggered by the acoustic cavitation of high-energy ultrasound promote the wetting between the reinforcement and the matrix, and lower the interfacial reaction temperature [18]. However, as the temperature is increased to 740 °C, a rapid increase in Al_3Ti content can be observed in the microstructure and the particle dimension reaches the micron-level (Fig. 5(c)). Therefore, we believe that the strong interfacial bonding is formed between Al_3Ti and Al when the pouring temperature reaches 720 °C. It plays a role in promoting the load transfer to Ti_3AlC_2 particles as well as interfacial strengthening, which is beneficial to the mechanical properties of the composite. Yet, as the temperature continues to rise, the coarser Al_3Ti significantly changes the stress distribution in the interfacial region, resulting in more stress transfer to the harder Al_3Ti and cracking in the near-interface region, which may weaken the mechanical properties of composite.

3.2 Mechanical properties

Figure 8 shows the Vickers hardness and tensile properties of the AT3.0 composite prepared at different pouring temperatures. Figure 8(a) reveals that the hardness of the composites generally shows an increasing trend with the increase of pouring temperature. AT3.0-740 °C composite has the maximum hardness of HV 73.8, an increase of 22.0% compared with AT3.0-700 °C composite. On the one hand, as the pouring temperature rises, the internal pore defects of the composites are reduced and the reinforcements are uniformly dispersed in the microstructure, further restraining the local matrix deformation and promoting more load transfer to the harder reinforcements [19]. On the other hand, the increase in pouring temperature accelerates the interfacial reaction between Al and Ti_3AlC_2, leading to an increase in the production of in-situ Al_3Ti. Herein, the hardness of Al_3Ti (6.0 GPa) [6] is greater than that of Ti_3AlC_2 (2.7 GPa) [20], so the hardness of the composite increases with the increase in pouring temperature.

The engineering tensile stress−strain curves of AT3.0 composites at different pouring temperatures are plotted in Fig. 8(b). Table 2 presents the results of Vickers hardness, elastic modulus, yield strength (YS), ultimate tensile strength (UTS) and elongation of each AT3.0 composite. The variation of tensile mechanical properties with temperature is also drawn in Figs. 8(c, d) to better understand the role of pouring temperature. It can be seen from Fig. 8(c) that the elastic modulus shows a tendency of increasing and then decreasing with the increase of pouring temperature, and the elastic modulus reaches a maximum of 75.6 GPa at 720 °C. In this study, the Ti_3AlC_2 particles are completely surrounded by the Al6061 melt, which lends itself to the Hashin−Shtrikman lower limit model (H−S lower model) to describe the theoretical elastic modulus of the composite [13,21].

$$E_c = E_m \times \frac{E_m V_m + E_r(V_r+1)}{E_r V_m + E_m(V_r+1)} \tag{3}$$

where E_c denotes the elastic modulus of composite, E_m, E_r, V_m and V_r represent the elastic moduli and volume fractions of Al6061 and Ti_3AlC_2, respectively, given the E_r of Ti_3AlC_2 is 297 GPa [6]. The red dashed line in Fig. 8(c) indicates the theoretical result of the H−S lower model (71.5 GPa), which is very close to the experimental value of AT3.0-700 °C. At 700 °C, the interface

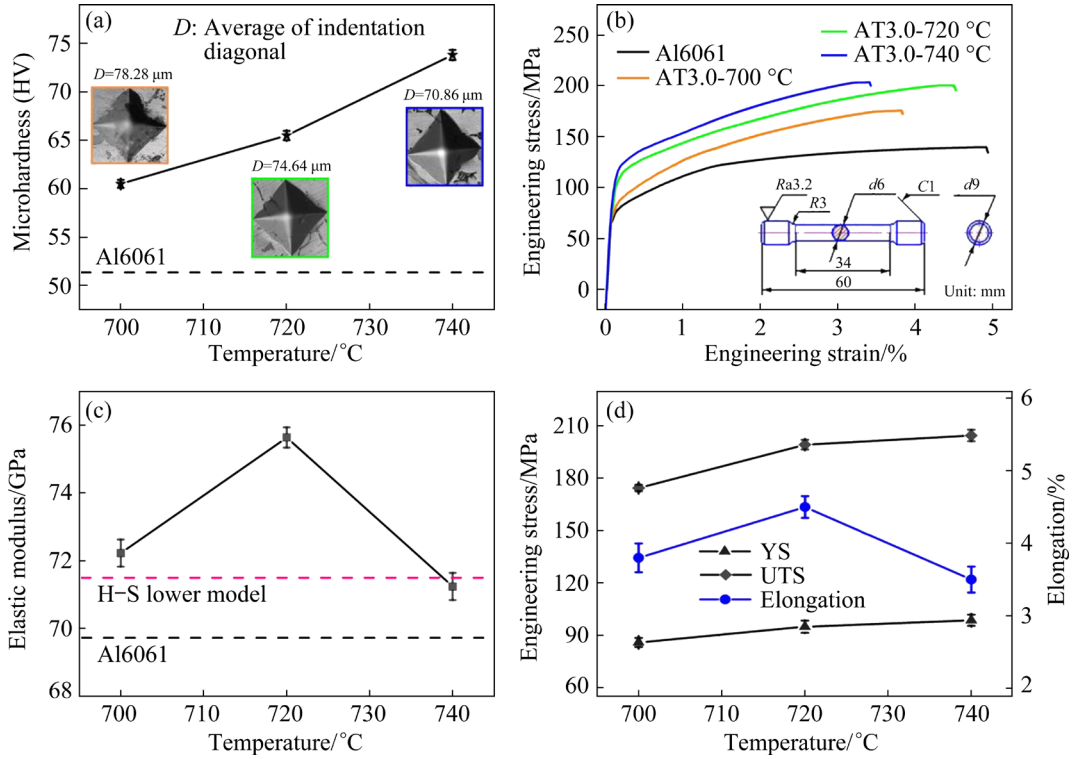

Fig. 8 (a) Vickers hardness; (b) Engineering tensile stress−strain curves of AT3.0 composites; (c) Elastic moduli variation curves; (d) Variation of YS, UTS and elongation

Table 2 Numerical results of Vickers hardness and tensile properties of each experimental material

Material	Vickers hardness (HV)	Modulus/GPa	Yield strength/MPa	Ultimate tensile strength/MPa	Elongation/%
Al6061-720 °C	51.3±0.3	69.7±0.2	72.5±1.9	140.7±2.3	4.9±0.2
AT3.0-700 °C	60.5±0.4	72.2±0.4	85.9±2.6	174.4±1.9	3.8±0.2
AT3.0-720 °C	65.5±0.5	75.6±0.3	94.9±3.5	199.2±2.8	4.5±0.2
AT3.0-740 °C	73.8±0.5	71.2±0.4	98.6±3.2	204.5±3.3	3.5±0.2

between the reinforcement and the matrix is nearly a non-reactive interfacial wetting, with a clean interface at this temperature. The matrix stress cannot be transferred to the reinforcements effectively, so the elastic modulus is relative low. With the increase of pouring temperature to 720 °C, a moderate interfacial reaction occurs at the interface of Al and Ti_3AlC_2. The fine in-situ Al_3Ti whiskers bond well with Al, improving the efficiency of load transfer at the interface, and the elastic modulus is also enhanced. Thereafter, the interfacial reaction intensifies and the grain size and yield of Al_3Ti increase rapidly, which improves the chance of interfacial cracks. In addition, Al_3Ti has a lower elastic modulus (216 GPa) [22] compared with Ti_3AlC_2, so the elastic modulus of AT3.0 composite decreases instead at this temperature.

The YS and UTS of AT3.0 composites generally show an increasing trend with increasing temperature, while the elongation reaches a maximum of 4.5% at 720 °C and then decreases with increasing temperature (Fig. 8(d)). At 720 °C, the YS, UTS and elongation of the composites increase by 10.4%, 14.2% and 17.5%, respectively, compared to 700 °C. Figure 9 shows the increments of UTS and elongation for AT3.0-720 °C and compares the strengthening effect of Ti_3AlC_2 or Al_3Ti particles on other Al alloys. It can be noted that with the addition of the reinforcement, the composites exhibit an improvement in strength at the expense of plasticity in general. In this work, AT3.0-720 °C has a UTS increment of 41.5% and elongation of −8.1% compared to Al6061 matrix, providing a significant increase in strength with only a slight decrease in plasticity. This is probably owing to the fact that the reinforcing phases play a role in impeding dislocation motion and inhibiting grain growth. Moreover, as the temperature increases to 720 °C, with a moderate interfacial reaction, the nano-sized Al_3Ti around the Ti_3AlC_2

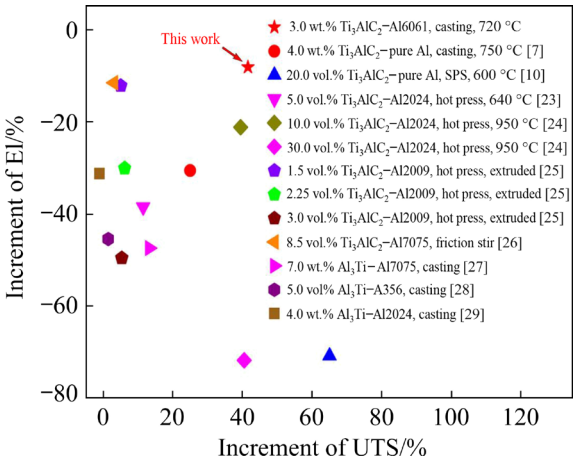

Fig. 9 Comparison of increment of UTS and elongation with other investigations

strengthens the bonding with Al matrix. Also, the dislocation density increases (Fig. 7(b)), which in turn improves the strength of the composite. As the temperature is further increased to 740 °C, the coarse Al_3Ti exerts a stronger hindering effect on dislocation motion due to its high hardness, and the strength continues to increase. However, the plasticity of the composites is somewhat compromised due to the further exposure of the brittleness of Al_3Ti.

The SEM images of the tensile fracture for AT3.0 composites at 700, 720 and 740 °C are shown in Fig. 10. At a pouring temperature of 700 °C, Ti_3AlC_2 shows obvious cleavage features in the lamellar orientation and is characterised by interfacial cracks with the Al matrix, indicating a weak interfacial bond (Fig. 10(a)). As the pouring temperature increases to 720 °C (Fig. 10(b)), no cracks are observed at the interface, with well bonded interfaces and a significant increase in dimple characteristics, reflecting better plasticity than that at 700 °C. For the fracture at 740 °C (Fig. 10(c)), visible coarse cracks could be observed near the rod-like particles, which could be the Al_3Ti particles detected in Fig. 4(c).

3.3 Mechanism

3.3.1 Interfacial reaction mechanism

A thermodynamic analysis of the possibility that Ti_3AlC_2 reacts with Al melt to form in-situ Al_3Ti is carried out. Based on the second law of thermodynamics and the solid−liquid phase change of the matrix during the interfacial reaction, the Gibbs free energy change ($\Delta G_{T_c}^{\Theta}$) for the reaction equation (2) can be expressed as [30]

$$\Delta G_{T_c}^{\Theta}=\Delta H_{T_0}^{\Theta}+\int_{T_0}^{T_c}\Delta C_p^{*}\mathrm{d}T-\Delta H_{\mathrm{fus}}(\mathrm{Al})-T_c(\Delta S_{T_0}^{\Theta}+\int_{T_0}^{T_c}\frac{\Delta C_p^{*}}{T}\mathrm{d}T-\frac{\Delta H_{\mathrm{fus}}(\mathrm{Al})}{T_{\mathrm{fus}}(\mathrm{Al})}) \quad (4)$$

where T_0 is the room temperature, T_c is the pouring temperature, T_{fus}(Al) is the fusion point of Al (933 K), ΔH_{fus}(Al) is the melting enthalpy of Al (10711 J/mol), ΔC_p^{*} is the the average reaction heat capacity of T_0 and T_c, and $\Delta H_{T_0}^{\Theta}$ and $\Delta S_{T_0}^{\Theta}$ are the standard molar enthalpy change, standard molar entropy change between products and reactants, respectively. Table 3 lists the enthalpy, entropy and heat capacity of each phase in the reaction system. The calculation shows that ΔG_{973}^{Θ} is −266.7 kJ at 700 °C, thus the Ti atoms on the surface of Ti_3AlC_2 may react with Al in the melt.

To analyse the effect of pouring temperature on the reaction rate, the Arrhenius model is used to explain the relationship between the atomic diffusion coefficient K_r and temperature T in the reaction system in terms of the reaction kinetics [34].

$$K_r=K_0\cdot\exp(-\frac{Q}{RT}) \quad (5)$$

where R is the gas molar constant (8.314 J/(mol·K)), K_0 is the diffusion constant (1.57×10^3 m/s), and Q is the effective activation energy (195.8 kJ/mol) [35]. Hereby, the diffusion coefficient is calculated to be 4.86×10^{-8} m/s at 700 °C, increasing by 1.6 and 2.6 times at 720 and 740 °C respectively. Thus, the higher the pouring temperature is, the greater the atomic thermal activation energy and the bigger inter-diffusion coefficient between Al atoms in the melt and Ti atoms in Ti_3AlC_2 are, which intensifies the reaction process and promotes the nucleation growth of Al_3Ti. The reaction between the Al melt and Ti at the edge of Ti_3AlC_2 is shown in Fig. 11. According to the Al−Ti phase diagram, the maximum equilibrium concentration of Ti in the Al melt is 0.13 at.% at 700 °C [36]. When the Ti content exceeds 0.13 at.%, a peritectic reaction occurs between Ti and Al. However, the small content of Ti_3AlC_2 added in this experiment and the low diffusion coefficient at 700 °C result in a weak reaction. As the temperature increases to 720 °C, the reaction intensifies due to the increase in diffusion coefficient and an accompanying increase in particle size and content of Al_3Ti, which in turn forms a nano-sized Al_3Ti transition layer

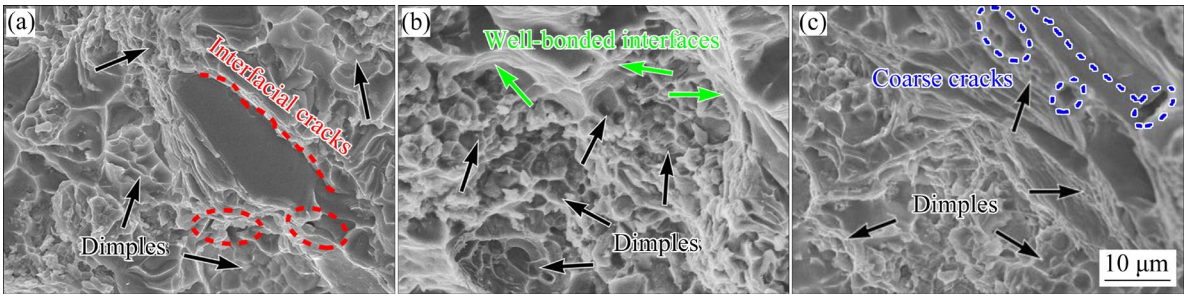

Fig. 10 SEM images of tensile fracture for AT3.0 composites at 700 °C (a), 720 °C (b) and 740 °C (c)

Table 3 Enthalpy, entropy, and heat capacity of each phase in interfacial reaction system

Phase	Enthalpy (298 K)/ (J·mol^{-1})	Entropy (298 K)/ (J·K^{-1}·mol^{-1})	Specific heat capacity (298 K)/(J·K^{-1}·mol^{-1})	Specific heat capacity (973 K)/(J·K^{-1}·mol^{-1})	Ref.
Al	0	28.3	24.3	31.7	[31]
Ti_3AlC_2	−427000	101.0	101.4	152.5	[32,33]
Al_3Ti	−142256	94.6	98.4	118.8	[31]
Al_4C_3	−207275	104.6	116.0	178.2	[31]

ΔH_{298}^{Θ}=−413854 J, ΔS_{298}^{Θ}=−148.0 J/K, ΔC_p^{*}=−5.25 J/K

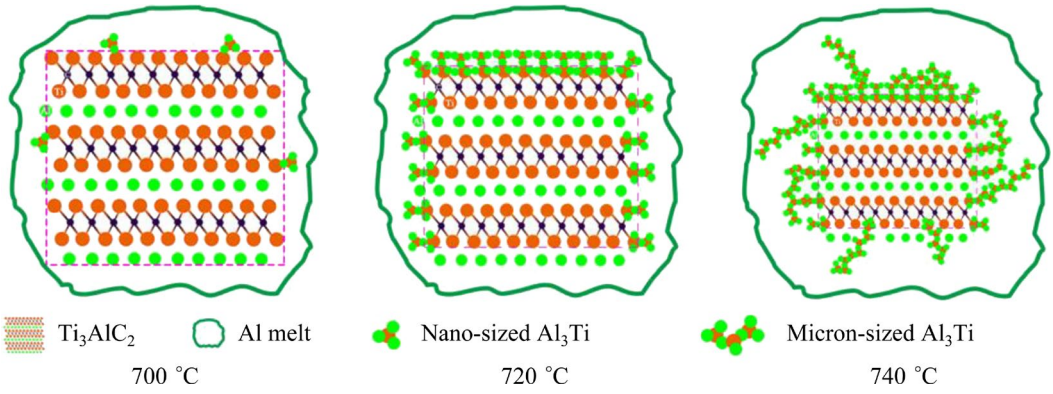

Fig. 11 Schematic illustration of reaction between Al melt and Ti at edge of Ti_3AlC_2

around the Ti_3AlC_2. Thereafter, the diffusion coefficient continues to increase with temperature and the Al_3Ti content and particle size are excessive. So, its brittleness adversely affects the performance of the composite. Therefore, 720 °C is considered to be the optimum interfacial reaction temperature.

3.3.2 Strengthening mechanism

The strength of AT3.0 composite achieves a large increase and maintains good plasticity at a pouring temperature of 720 °C. It is likely that Ti_3AlC_2 and the nano-sized Al_3Ti generated at this temperature play a synergistic role on the composite by grain refinement strengthening ($\Delta\sigma_{GR}$), load transfer strengthening ($\Delta\sigma_{LT}$), and thermal mismatch strengthening ($\Delta\sigma_{CTE}$). Hereby, model calculations are performed to analyse the contribution of different strengthening mechanisms on the yield strength.

The uniformly dispersed Ti_3AlC_2 particles can effectively inhibit the growth of α(Al) grains, thus improving the mechanical properties of the composite. Herein, the Hall−Petch model is usually used to calculate the improvement of yield strength by grain refinement [37].

$$\Delta\sigma_{GR}=\lambda\left(d_{com}^{-1/2}-d_{m}^{-1/2}\right) \tag{6}$$

where λ is the Hall−Petch constant of 74 MPa·μm$^{1/2}$ for Al [38], and d_{com} and d_m are the average grain sizes of the composite and Al6061 matrix, respectively.

Both Ti_3AlC_2 and their surrounding in-situ Al_3Ti particles can improve the yield strength by means of transferring loads. As shown in Figs. 5 and 7, Al_3Ti is mainly dispersed at the edges of some Ti_3AlC_2 particles, and partially scattered in the matrix under acoustic cavitation to act as a non-homogeneous nucleation core. Hence, the increase in yield strength caused by load transfer strengthening can be expressed as [39]

$$\Delta\sigma_{LT}=\varphi V_r\sigma_m \tag{7}$$

where φ and V_r refer to the aspect ratio and volume fraction of the reinforcement, respectively, and σ_m denotes the yield strength of the Al6061 matrix.

The difference in thermal expansion coefficient (CTE) between the matrix and reinforcing phases triggers lattice distortion near the interface when the composite is subjected to plastic deformation, and then generating a higher dislocation density. Moreover, to accommodate the difference in CTE, geometric dislocations are spontaneously generated around the reinforcing phases, thus increasing the flow stress of the matrix. Figure 12 shows the dark-field TEM morphology of AT3.0-720 °C composite. A large number of dislocations are generated around the Ti_3AlC_2 particles (Fig. 12(a)), and dislocation accumulation around the nascent Al_3Ti phases can also be seen in Fig. 12(b). The CTE of pure Al (23×10^{-6} K^{-1}) [40] is greater than that of Ti_3AlC_2 (9.2×10^{-6} K^{-1}) and Al_3Ti (15×10^{-6} K^{-1}) [23], implying that both phases play an important role in the thermal mismatch strengthening. The strengthening induced by thermal mismatch can be calculated by the following model [41]:

$$\Delta\sigma_{CTE}=\alpha Mb\sqrt{\rho} \tag{8}$$

$$\rho=12\Delta\beta\Delta T V_r/[bd(1-V_r)] \tag{9}$$

where α is the constant (~1.25) [41], M is the shear modulus of Al6061 (~26 GPa), b is the amplitude of Burgers vector of Al (0.286 nm) [42], $\Delta\beta$ is the CTE mismatch between Al and reinforcement, ΔT

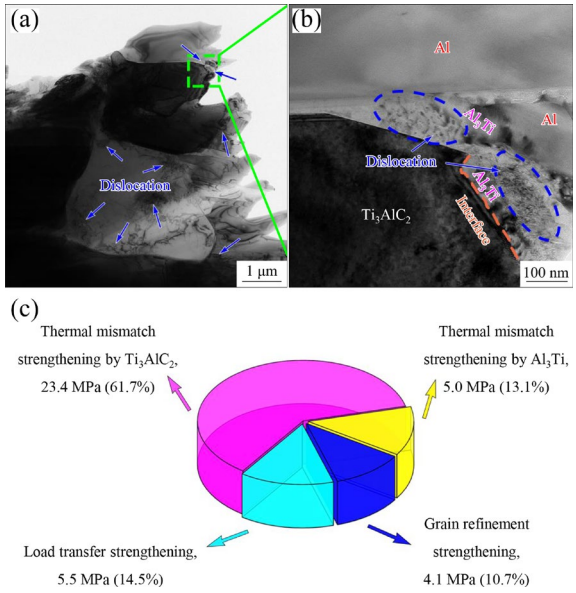

Fig. 12 Dark-field TEM images: (a) Low magnification; (b) Enlarged view of green zone in (a); (c) Contribution of each strengthening mechanism

is the temperature variation from pouring temperature to room temperature, and d is the average size of reinforcement.

In summary, increments are calculated for the various strengthening models of the AT3.0-720 °C composite. Wherein, the thermal mismatch strengthening plays a dominant role with a contribution of about 74.8%. Then the second phase strengthening follows with a contribution of about 14.5%, and thereafter, the grain refinement strengthening with a contribution of about 10.7%. The results of the contribution rate of each strengthening mechanism are presented in Fig. 12(c).

The effects of the interfacial bonding state between the reinforcement phases and the Al matrix on the mechanical properties are further explored by analyzing the changes in the interfacial reaction of Ti_3AlC_2 at temperatures of 700, 720 and 740 °C, as shown in Fig. 13. A weak interfacial bonding can be observed in Fig. 13(a) (700 °C), where the interface between Ti_3AlC_2 and Al is clear. When subject to external stresses leading to plastic deformation, it can only be absorbed by the deformation of Ti_3AlC_2, while excessive stress transfer can cause interfacial cracking before its deformation (Fig. 13(d)). As the temperature increases to 720 °C, the interfacial reaction at the edge of Ti_3AlC_2 particles increases, forming a fine, well-bonded transition layer (Fig. 13(b)). At this point, the nano-sized in-situ Al_3Ti can effectively absorb the interfacial stress and promote the transfer of stress to Ti_3AlC_2 sufficiently (Fig. 13(e)), thus exhibiting better strength and the highest elongation. Subsequently, with the increase of pouring temperature, Al atoms rapidly diffuse into Ti_3AlC_2 particles and continue to react with Ti atoms, resulting in a large number of rod-shaped Al_3Ti

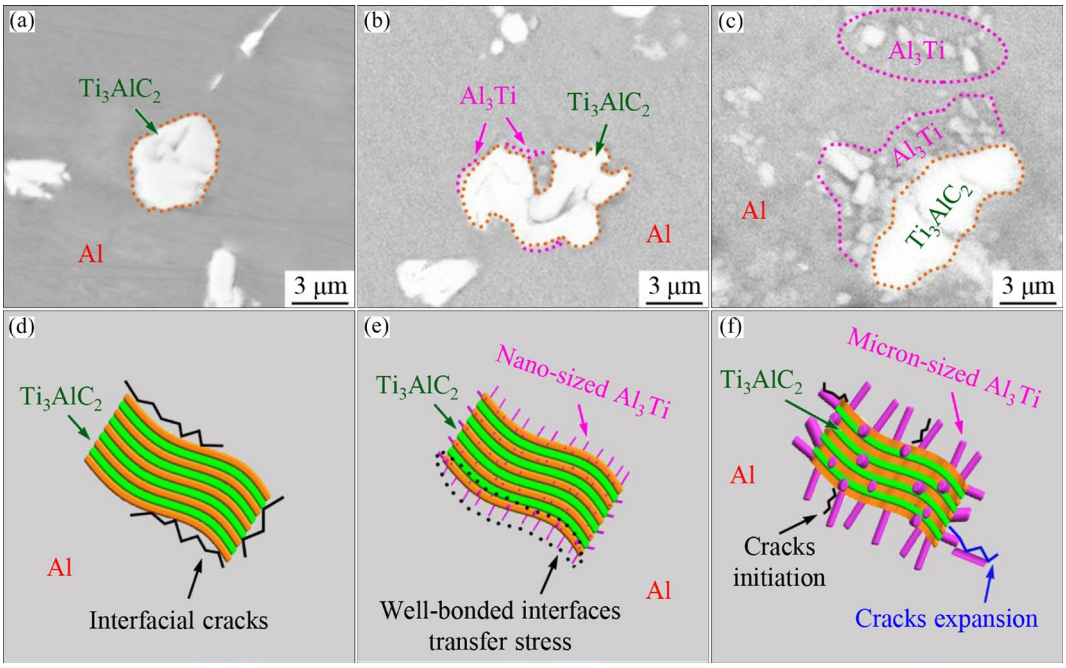

Fig. 13 SEM morphologies (a−c) and schematics (d−f) of interfacial bonding between Al and Ti_3AlC_2: (a, d) 700 °C; (b, e) 720 °C; (c, f) 740 °C

formed and splitting the Al−Ti_3AlC_2 interface (Fig. 13(c)). In this case, more stress is absorbed by the harder Al_3Ti. However, the brittle nature of Al_3Ti makes it more likely to be a source of crack initiation and induces crack expansion along the micron-sized Al_3Ti particles (Fig. 13(f)), leading to an increase in strength but a significant decrease in plasticity. Consequently, excellent comprehensive mechanical properties of AT3.0-720 °C composite are inextricably linked to the interfacial bonding state.

4 Conclusions

(1) At a content of 3.0 wt.% Ti_3AlC_2, the grain size of α(Al) in the Ti_3AlC_2-Al6061 composite is optimal, with a reduction of 50.1% compared with Al6061 matrix.

(2) At 720 °C, a nano-sized Al_3Ti transition layer is generated around the edge of Ti_3AlC_2 particles in AT3.0 composite, forming a well-bonded Al−Al_3Ti interface, which effectively accumulates interfacial dislocations and transfers interfacial stresses.

(3) The UTS of the composites shows an overall increasing trend with increasing pouring temperature. The UTS of AT3.0-720 °C is increased by 41.5% compared with Al6061 matrix, but the elongation decreases slightly.

CRediT authorship contribution statement

Zhi-bin LIU: Investigation, Methodology, Visualization, Writing − Original draft; **Jia-bao BAO:** Investigation, Data curation; **Wen-jie HU:** Investigation, Software; **Hong YAN:** Conceptualization, Supervision, Writing − Reviewing and editing.

Declaration of competing interest

The authors declare that they have no known competing financial interests or personal relationships that could have appeared to influence the work reported in this paper.

Acknowledgments

This study was financially supported by the National Natural Science Foundation of China (No. 51965040), and Science and Technology Project of Jiangxi Provincial Department of Transportation, China (No. 2022H0048).

References

[1] LI Nai-yong, MAO Wei-min, GENG Xiao-xin. Preparation of semi-solid 6061 aluminum alloy slurry by serpentine channel pouring [J]. Transactions of Nonferrous Metals Society of China, 2022, 32: 739−749.

[2] XIE Ke-wei, NIE Jin-feng, HU Kai-qi, MA Xia, LIU Xiang-fa. Improvement of high-temperature strength of 6061 Al matrix composite reinforced by dual-phased nano-AlN and submicron-Al_2O_3 particles [J]. Transactions of Nonferrous Metals Society of China, 2022, 32: 3197−3211.

[3] LI Jian-yu, LV Shu-lin, CHEN Lu, LIAO Qiao, GUO Wei, WU Shu-sen. Influence of squeeze casting pressure on nanoparticle distribution and mechanical properties of nano-SiC_p/Al−Cu composites assisted with ultrasonic vibration [J]. Transactions of Nonferrous Metals Society of China, 2023, 33: 1977−1987.

[4] WANG Yang, LIU Qiang, ZHANG Biao, ZHANG Hao-qian, JIN Yi-cheng, ZHONG Zhao-xin, YE Jian, REN Yu-han, YE Feng, WANG Wen. Developing nacre-inspired laminate-reticular 2024Al/B_4C composites with high damage resistance by adjusting compositional wettability [J]. Transactions of Nonferrous Metals Society of China, 2022, 32: 1105−1118.

[5] YANG De-xuan, ZHOU Yu, YAN Xing-heng, WANG Hong-lei, ZHOU Xin-gui. Highly conductive wear resistant Cu/Ti_3SiC_2 (TiC/SiC) co-continuous composites via vacuum infiltration process [J]. Journal of Advanced Ceramics, 2020, 9: 83−93.

[6] WANG Xiao-hui, ZHOU Yan-chun. Layered machinable and electrically conductive Ti_2AlC and Ti_3AlC_2 ceramics: A review [J]. Journal of Materials Science & Technology, 2010, 26: 385−416.

[7] ZHAI Wen-yan, PU Bo-wei, SUN Liang, XU Liu-jie, WANG Yi-ran, HE Lin, DONG Hui, GAO Yi-min, HAN Man-man, XUE Yi-song. Influence of Ti_3AlC_2 content and load on the tribological behaviors of Ti_3AlC_2p/Al composites [J]. Ceramics International, 2022, 48: 1745−1756.

[8] WANG Wen-jing, GAUTHIER-BRUNET V, BEI Guo-ping, LAPLANCHE G, BONNEVILLE J, JOULAIN A, DUBOIS S. Powder metallurgy processing and compressive properties of Ti_3AlC_2/Al composites [J]. Materials Science and Engineering A, 2011, 530: 168−173.

[9] WANG Yuan-bo, HUANG Zhen-ying, HU Wen-qiang, CAI Le-ping, LEI Cong, YU Qun, JIAO Yi-dan. Preparation and characteristics of Ti_3AlC_2−Al_3Ti/Al composite materials synthesized from pure Al and Ti_3AlC_2 powders [J]. Materials Characterization, 2021, 178: 111298.

[10] WANG Zhi-jun, MA Yi-fu, SUN Kai, ZHANG Qiang, ZHOU Chang, SHAO Pu-zhen, XIU Zi-yang, WU Gao-hui. Enhanced ductility of Ti_3AlC_2 particles reinforced pure aluminum composites by interface control [J]. Materials Science and Engineering A, 2022, 832: 142393.

[11] SUN Yue, ZHOU Chang, ZHAO Zi-min, YU Zhen-he, WANG Zhi-jun, LIU Hao, ZHANG Ning-bo, YANG Wen-shu, WU Gao-hui. Microstructure and mechanical properties of Ti_2AlC particle and in-situ $TiAl_3$ reinforced pure

Al composites [J]. Materials Science and Engineering A, 2020, 785: 139310.

[12] AI Ming-xing, ZHAI Hong-xiang, ZHOU Yang, TANG Zhao-yun, HUANG Zhen-ying, ZHANG Zhi-li, LI Shi-bo. Synthesis of Ti_3AlC_2 powders using Sn as an additive [J]. Journal of the American Ceramic Society, 2006, 89: 1114−1117.

[13] YU Wen-bo, WANG Xiao-jun, ZHAO Hong-bin, DING Chao, HUANG Zhen-ying, ZHAI Hong-xiang, GUO Zhi-peng, XIONG Shou-mei. Microstructure, mechanical properties and fracture mechanism of Ti_2AlC reinforced AZ91D composites fabricated by stir casting [J]. Journal of Alloys and Compounds, 2017, 702: 199−208.

[14] SU Yu-wu, ZHANG Chao, LIU Shan-shan, PANG Liang-yue, LIN Huan-cai, ZHI Qing-hui. Effect of thermal cycling aging on the surface microhardness and roughness of resin-infiltrated enamel lesions [J]. Science of Advanced Materials, 2021, 13: 356−363.

[15] KHALILI V, HEIDARZADEH A, MOSLEMI S, FATHYUNES L. Production of Al6061 matrix composites with ZrO_2 ceramic reinforcement using a low-cost stir casting technique: Microstructure, mechanical properties, and electrochemical behavior [J]. Journal of Materials Research and Technology, 2020, 9: 15072−15086.

[16] LI Nai-yong, MAO Wei-min, GENG Xiao-xin, ZHANG Rong-sheng, YAN Bing-dong. Microstructure, segregation and fracture behavior of 6061 aluminum alloy samples formed by semi-solid or traditional high pressure die casting [J]. Materials Today Communications, 2022, 31: 103418.

[17] ZHANG Jie, WANG Jing-yang, ZHOU Yan-chun. Structure stability of Ti_3AlC_2 in Cu and microstructure evolution of Cu−Ti_3AlC_2 composites [J]. Acta Materialia, 2007, 55: 4381−4390.

[18] GUAN Feng, JIANG Wen-ming, WANG Jun-long, LI Guang-yu, ZHANG Zheng, FAN Zi-tian. Development of high strength Mg/Al bimetal by a novel ultrasonic vibration aided compound casting process [J]. Journal of Materials Processing Technology, 2022, 300: 117441.

[19] ANASORI B, CASPI E N, BARSOUM M W. Fabrication and mechanical properties of pressureless melt infiltrated magnesium alloy composites reinforced with TiC and Ti_2AlC particles [J]. Materials Science and Engineering A, 2014, 618: 511−522.

[20] GUPTA R, CHAUDHARI G P, DANIEL B S S. Strengthening mechanisms in ultrasonically processed aluminium matrix composite with in-situ Al_3Ti by salt addition [J]. Composites Part B: Engineering, 2018, 140: 27−34.

[21] HASHIN Z, SHTRIKMAN S. A variational approach to the theory of the elastic behaviour of multiphase materials [J]. Journal of the Mechanics and Physics of Solids, 1963, 11: 127−140.

[22] NAKAMURA M, KIMURA K. Elastic constants of $TiAl_3$ and $ZrAl_3$ single crystals [J]. Journal of Materials Science, 1991, 26: 2208−2214.

[23] ZHUANG Wei-ci, HUANG Zhen-ying, HU Wen-qiang, WANG Yuan-bo, WU You-bo, YU Qun, WANG Hong-jie, LI Xue. Microstructure characterization and enhanced mechanical properties of quasi-continuous network structured Ti_3AlC_2−Al_3Ti/2024Al composite [J]. Materials Characterization, 2022, 191: 112131.

[24] WANG Yuan-bo, HUANG Zhen-ying, HU Wen-qiang, YU Qun, WANG Hong-jie, LI Xue, DASTAN D, ZHOU Yang. Microstructure and mechanical behaviors of Ti_3AlC_2 triggered in-situ Al_3Ti and TiC reinforced 2024Al composite [J]. Journal of Materials Research and Technology, 2022, 19: 289−299.

[25] LI X N, LI P Y, LIU Z Q, MA K, LIU Z Y, XIAO B L, MA Z Y. Microstructure and mechanical properties of Ti_3AlC_2 reinforced Al−4.5Cu−1.5Mg composites fabricated by powder metallurgy [J]. Journal of Materials Science, 2023, 58: 2570−2580.

[26] AHMADIFARD S, MOMENI A, BAHMANZADEH S, KAZEMI S. Microstructure, tribological and mechanical properties of Al7075/Ti_3AlC_2 MAX-phase surface composite produced by friction stir processing [J]. Vacuum, 2018, 155: 134−141.

[27] SUJITH S V, KIM H, MULIK R S, PARK H, LEE J. Synergistic effect of in-situ Al-7075/Al_3Ti metal matrix composites prepared via stir-assisted ultrasonic melt processing under dynamic nucleation [J]. Metals and Materials International, 2022, 28: 2288−2303.

[28] MA Si-ming, WANG Xiao-ming. Mechanical properties and fracture of in-situ Al_3Ti particulate reinforced A356 composites [J]. Materials Science and Engineering A, 2019, 754: 46−56.

[29] CHEN Gang, JIN Yu, ZHANG Hong-ming, HAN Fei, CHEN Qiang, XU Jun-rui, ZHAO Zu-de. Microstructures and mechanical properties of in-situ Al_3Ti/2024Al composites after solution and subsequent aging treatment [J]. Materials Science and Engineering A, 2018, 724: 181−188.

[30] MORTIMER R G. Physical chemistry [M]. San Diego: Harcourt/Academic Press, 2000.

[31] BINNEWIES M, MILKE E. Thermochemical Data of Elements and Compounds [M]. Weinheim: Wiley-VCH Verlag Gmbh, 2002.

[32] WITUSIEWICZ V T, HALLSTEDT B, BONDAR A A, HECHT U, SLEPTSOV S V, VELIKANOVA T Y. Thermodynamic description of the Al−C−Ti system [J]. Journal of Alloys and Compounds, 2015, 623: 480−496.

[33] SHAHIN N, KAZEMI S, HEIDARPOUR A. Mechanochemical synthesis mechanism of Ti_3AlC_2 MAX phase from elemental powders of Ti, Al and C [J]. Advanced Powder Technology, 2016, 27: 1775−1780.

[34] SMIALEK J L. Oxygen diffusivity in alumina scales grown on Al-MAX phases [J]. Corrosion Science, 2015, 91: 281−286.

[35] ZHANG Jian-yu, WANG Yan-hui, LU Zheng, CHEN Qing-an, CHEN Ya-yu, LI He-zong. Formation mechanism and growth kinetics of $TiAl_3$ phase in cold-rolled Ti/Al laminated composites during annealing [J]. Transactions of Nonferrous Metals Society of China, 2022, 32: 524−539.

[36] SCHUSTER J C, PALM M. Reassessment of the binary aluminum-titanium phase diagram [J]. Journal of Phase Equilibria and Diffusion, 2006, 27: 255−277.

[37] LIU Lu, YING Guo-bing, WEN Dong, LI Yue-xia, ZHANG Kai-cheng, MIN Hui-hua, HU Cong, SUN Cheng, WANG

Cheng. High-performance copper-matrix materials reinforced by nail board-like structure 2D Ti_3C_2Tx MXene with in-situ TiO_2 particles [J]. Materials Science and Engineering A, 2022, 832: 142392.

[38] LI Qiang, QIU Feng, DONG Bai-Xin, GENG Run, LV Ming-ming, ZHAO Qian-long, JIANG Qi-chuan. Fabrication, microstructure refinement and strengthening mechanisms of nanosized SiC_P/Al composites assisted ultrasonic vibration [J]. Materials Science and Engineering A, 2018, 735: 310−317.

[39] WU Xiao-feng, XU Chun-xiang, ZHANG Zheng-wei, YANG Wen-fu, ZHANG Jing-shan. Microstructure evolution, strengthening mechanisms and deformation behavior of high-ductility Mg−3Zn−1Y−1Mn alloy at different extrusion temperatures [J]. Transactions of Nonferrous Metals Society of China, 2023, 33: 422−437.

[40] ELOMARI S, BOUKHILI R, MARCHI C S, MORTENSEN A, LLOYD D J. Thermal expansion responses of pressure infiltrated SiC/Al metal-matrix composites [J]. Journal of Materials Science, 1997, 32: 2131−2140.

[41] LUO Si-wei, WU Yue, CHEN Biao, SONG Min, YI Jian-hong, GUO Bai-song, WANG Qi-wei, YANG Yong, LI Wei, YU Zhen-tao. Effects of Cu content on microstructures and compressive mechanical properties of CNTs/Al-Cu composites [J]. Transactions of Nonferrous Metals Society of China, 2022, 32: 3860−3872.

[42] SRIVASTAVA N, CHAUDHARI G P. Strengthening in Al alloy nano composites fabricated by ultrasound assisted solidification technique [J]. Materials Science and Engineering A, 2016, 651: 241−247.

Ti_3AlC_2 增强 Al6061 复合材料的显微组织、界面反应及力学性能

刘智彬[1,2]，鲍家宝[1]，胡文杰[1]，闫 洪[1]

1. 南昌大学 先进制造学院，南昌 330031；
2. 江西交通职业技术学院，南昌 330013

摘 要：研究 Al 和 Ti_3AlC_2 在不同浇铸温度下的界面反应及其对复合材料显微组织和力学性能的影响。结果表明，与 Al6061 基体相比，添加 3.0% (质量分数)Ti_3AlC_2 可使复合材料中 α(Al)的平均晶粒细化 50.1%。形貌分析表明，当浇注温度为 720 ℃时，在 Ti_3AlC_2 边缘生成厚度约为 180 nm 的原位 Al_3Ti 过渡层，形成结合良好的 Al−Al_3Ti 界面。在此温度下，Al6061−3.0%Ti_3AlC_2(质量分数)复合材料的极限抗拉强度为 199.2 MPa，比 Al6061 基体提高 41.5%。机理分析进一步阐明，浇注温度为 720 ℃有利于在 Ti_3AlC_2 边缘生成纳米级过渡层。此状态下，热错配强化起主导作用，其强化贡献率约为 74.8%。

关键词：Al6061 复合材料；Ti_3AlC_2；显微组织；界面反应；拉伸力学性能

(Edited by Xiang-qun LI)